Correspondence to:
D. Florez,
darien_florez@brown.edu

Modeling Lunar Pyroclasts to Probe the Volatile Content of the Lunar Interior

Darien Florez[1] [ID], **Christian Huber[1]** [ID], **Ralph E. Milliken[1]** [ID], and **Julia Berkson[1]**

[1]Department of Earth, Environmental and Planetary Sciences, Brown University, Providence, RI, USA

Abstract Constraining the volatile budget of the lunar interior has important ramifications for models of Moon formation. While many early and previous measurements of samples acquired from the Luna and Apollo missions suggested the lunar interior is depleted in highly volatile elements like H, a number of high-precision analytical studies over the past decade have argued that it may be more enriched in water than previously thought. Here, we integrate recent remotely sensed near-infrared reflectance measurements of small Dark-Mantle-Deposits (DMDs) Birt E and Grimaldi, interpreted to represent pyroclastic deposits, and physics-based eruption models to better constrain the preeruptive water content of the magmas that resulted in these deposits. We model the trajectory and water loss of pyroclasts from eruption to deposition, coupling eruption dynamics with a volatile diffusion model for each pyroclast. Modeled pyroclast sizes and final water contents are then used to predict spectral reflectance properties for comparison with the observed orbital near-infrared data. We develop an inversion scheme based on the Markov-Chain Monte-Carlo (MCMC) method to retrieve constraints between governing parameters such as the initial volatile content of the melt and the pyroclast size distribution (which influences the remotely measured water absorption strengths). The MCMC inversion allows us to estimate the primordial (preeruption) water content for different DMDs and therefore explore whether their source is volatile-rich. Our results suggest that the preeruptive water content of the magmas sampled by Birt E and Grimaldi can be constrained within a range 400–800 ppm, while the pyroclast size in diameter corresponding to the 50th percentile of a given deposit likely ranges from ~400 to 600 μm in diameter. Finally, we determine the evaporation and cooling rates are likely low, ~10^{-6} m/s and 6°C/s, respectively.

1. Introduction

Several models of lunar formation that have recently gained momentum in the planetary science community involve, to an extent, the giant impact theory (e.g., the terrestrial synestia model of Lock et al. (2018)). In this giant impact theory, the Moon is thought to have been formed from the coalescence of debris from a collision between an impactor and a proto-Earth (Canup, 2004), leading to the formation of a lunar magmatic ocean and the large-scale degassing of the Moon (Lucey et al., 2006). The depletion of hydrogen (e.g., in the form of OH/H_2O, hereafter referred to simply as "water" or H_2O) in volcanic samples returned from Luna and Apollo missions seemed to support this, but a growing body of research now suggests that the lunar mantle, or at least some parts of the lunar mantle, may not be as severely depleted in water as previously thought (Boyce et al., 2010; Greenwood et al., 2011; Hauri et al., 2011; Hui et al., 2017; McCubbin et al., 2010a, 2010b; Rutherford et al., 2017; Saal et al., 2008, 2013).

Much of the uncertainty surrounding the character of the lunar interior stems from the availability of direct samples from the lunar surface being limited to only a small number of locations. However, telescopic and other remote sensing observations have revealed so-called Dark-Mantle-Deposits (DMDs) to be distinct features across the lunar surface (Gaddis et al., 1998, 2000, 1985, 2003; Gustafson et al., 2012; Head, 1974; Weitz et al., 1998). Although most large DMDs have not been sampled (an exception being material collected on the edge of the Taurus-Littrow DMD during Apollo 17), and in general the relation of many DMDs to the pyroclastic materials returned from the Luna and Apollo missions is unclear, they are interpreted to be pyroclastic in nature. If true, materials in these deposits represent magmas sourced from the deep lunar interior (Gaddis et al., 1985; Head, 1974; Weitz et al., 1998).

Much recent work to understand the dissolved water in lunar magmas and their source regions has focused on the water in lunar apatites (Greenwood et al., 2011; Robinson et al., 2016; Tartese et al., 2013, 2014). Additionally, the prefragmentation water content of different lunar magmas has been studied using picritic glasses (Hauri et al., 2011; Rutherford et al., 2017; Saal et al., 2008, 2013). The latter offers the advantage that it can be used in concert with remotely sensed data of lunar pyroclastic deposits and is the focus of this paper.

These glasses are thought to have been emplaced through Hawaiian-like, fire-fountaining eruptions (Wilson & Head, 2003) and include green (low-Ti), yellow (intermediate Ti), and orange, red, and black glasses (high-Ti). They represent quenched melts that are ultramafic in composition (Delano, 1986; Saal et al., 2008), crystal poor (Delano, 1986; Saal et al., 2008), were erupted as fine beads (<1 mm) (Delano, 1986; Heiken & McKay, 1977; Longhi, 1992; Saal et al., 2008; Weitz et al., 1998), and are believed to have been generated from magmas sourced at depths of 300–500 km (Delano, 1980; Delano & Lindsley, 1983; Elkins et al., 2000; Elkins-Tanton et al., 2003; Longhi, 2006; Shearer & Papike, 1993; Shearer et al., 2006). For this reason, they have been used to probe the volatile content of parts of the lunar interior by virtue of melt inclusions, diffusion modeling, and through solubility experiments (Hauri et al., 2011; Rutherford et al., 2017; Saal et al., 2008, 2013).

Volatile content profiles of individual picritic glass beads were first reported by Saal et al. (2008), where improvements in secondary ion mass spectrometry allowed for lower detection threshold for water. These improvements led to the detection of measurable amounts of water (up to 46 ppm), and Saal et al. (2008) found systematic depletion from core to rim within individual beads. These volatile profiles suggest the beads degassed during ascent and eruption (Saal et al., 2008), consistent with a volcanic (as opposed to impact) origin. The trace amount of water detected in these glasses therefore represents the concentration of water in the parental magma upon fragmentation after magmatic degassing.

Magmatic degassing is assumed to take place as fragmented pyroclasts travel through a thermally opaque, water undersaturated, gas cloud during their ballistic trajectory (Wilson & Keil, 2012). The volatile profiles recorded by these pyroclasts during this process are therefore modulated by the cooling time (i.e., the time spent traveling through the opaque gas cloud), the size and shape of the pyroclast, and the preeruption magmatic volatile content, as well as the conditions (rate) above the blocking temperature (Crank, 1975). Here, the blocking temperature is generally assumed to be the melt-glass transition temperature for the volatile species considered. Based on these relationships, the volatile profiles measured in the pyroclasts can be used to constrain the range of values for these different parameters. For instance, Saal et al. (2008) applied the measured volatile content values to a degassing/diffusion model and estimated the initial amount of water upon magma fragmentation to be within the range of 260 to 15,000 ppm (Saal et al., 2008) (94.0% and 99.9% water loss, respectively), with a best fitting solution of 745 ppm (98% water loss). Though even the lowest model values have a significant implication for the volatile budget of the Moon, this is a broad range and the solution is clearly not unique. Therefore, further constraints are desired to help narrow down the range of possible solutions and provide useful estimates of the prefragmentation volatile content of the magmas that feed pyroclastic eruptions on the Moon.

One useful additional constraint is, when possible, to locate the vent(s) associated with a pyroclastic deposit. The size of a pyroclastic deposit and the distance from the point of origin (vent) provides information on the trajectory of the pyroclasts and thus their cooling time above the blocking temperature. Unfortunately, specific vents associated with glass beads returned from the Luna and Apollo sampling sites are not apparent in existing data. However, remotely sensed data such as images from NASA's Lunar Reconnaissance Orbiter have revealed the presence of vents for several small DMDs elsewhere on the lunar surface (Gustafson et al., 2012). Two of these DMDs are Grimaldi and Birt E (Besse et al., 2014). In addition to exhibiting possible vents, the vents themselves for these two DMDs are surrounded by concentric deposits with lower albedos at visible wavelengths (Besse et al., 2014). Additionally, the deposits exhibit distinct spectral signatures consistent with volcanic glass signature when compared with surrounding lava flows (Besse et al., 2014). These features are indicative of pyroclastic emplacement and, along with the spectral signatures indicating 71–77 wt % glass in the deposits (Trang et al., 2017), make them appealing candidates for studying different aspects of lunar volcanism.

Interestingly, near-infrared reflectance spectra acquired by the Moon Mineralogy Mapper (M3) imaging spectrometer on the Chandrayaan-1 spacecraft have revealed that nearly all DMDs on the Moon exhibit spectral signatures indicative of enhanced water contents, including Grimaldi, Birt E, and several other small DMDs with visible vents (Li & Milliken, 2017; Milliken & Li, 2017).

The M3 reflectance spectra, in conjunction with laboratory measurements and radiative transfer models, were used to estimate the amount of water in the DMDs based on the strength of an OH/H_2O absorption feature at a wavelength of ~2.7–2.9 μm (Milliken and Li, 2017). The parameter used to characterize the absorption strength was the Effective Single Particle Absorption Thickness (ESPAT) as described and defined by (Hapke et al., 1993). Previous studies have shown that the ESPAT parameter is linearly correlated with water content for a wide range of hydrous materials, but the slope of that linear relationship varies with the particle size of the material (Li & Milliken, 2017; Milliken, 2006; Milliken & Li, 2017; Milliken & Mustard, 2005, 2007a, 2007b). In order to estimate the current (postemplacement) water content of the DMDs, Milliken and Li (2017) assumed the deposits were spectrally dominated by particles (pyroclasts) ~60–80 μm in diameter. The main challenges with this approach are (1) that the pyroclast size distribution of the deposits as a whole, as well as the pyroclast size distribution with distance from the vent, are unknown, and (2) that volatile diffusion profiles for glass beads within these deposits are unavailable and therefore cannot be used to independently determine the prefragmentation water content.

In this study, we seek to determine if there exist a suite of conditions for which analytical measurements of lunar glasses, physical eruption models, and remotely sensed measurements of pyroclastic deposits yield self-consistent results for water in lunar DMDs. That is, can pyroclast size distributions and water content values estimated from an eruption model be used to predict the range of possible absorption strengths (ESPAT values) that might be observed in near-infrared reflectance spectra and are these in agreement with the values reported in Milliken and Li (2017)? Alternatively, do eruption models predict pyroclast sizes significantly larger or smaller than assumed in that previous study and, if so, what does this imply about quantifying water content of DMDs using near-infrared reflectance data such as M³? To address these issues and further constrain prefragmentation water content of lunar magmas, we develop a new approach using eruption dynamics together with volatile diffusion out of pyroclasts. Near-IR ESPAT values are expected to vary as a function of both water content and pyroclast size (Li & Milliken, 2017; Milliken & Li, 2017). As such, transects of ESPAT values from a DMD vent to its perimeter are expected to vary based on differences in prefragmentation water content, pyroclast size, and the exsolved gas content that accelerates the pyroclasts to their eventual deposition. All three of these critical parameters can be independently evaluated in a physics-based eruption model, and we use ESPAT profiles measured across the DMDs Birt E and Grimaldi to find a solution space that results in fits to the ESPAT profiles while simultaneously satisfying the dynamics of volcanic events on the Moon. To accomplish this, we develop an approach that requires calculating water loss through magmatic diffusion in pyroclasts and the loss is calculated here using new constraints from diffusion modeling of analytically measured picritic glasses similar to that of Saal et al. (2008). This study represents the first time that analytical measurements of lunar glasses, a physics-based eruption model, and remote sensing observations of lunar water absorptions have all been integrated to better constrain the prefragmentation water content of the parental magmas of different lunar DMDs.

2. Methods

To investigate the volatile budget of DMD magmas, we couple an eruption model for pyroclast dispersal with a diffusion model to account for volatile loss during pyroclast transport above the blocking temperature. The eruption model simulates the ballistic trajectories of pyroclasts from fragmentation to deposition. The deposition of pyroclasts within a vacuum from eruptions of fire-fountain, vulcanian, and strombolian nature are expected to behave in this way (i.e., Hawke et al., 1989; Wilson, 1972). However, the model assumes fragmentation driven by the ascent and decompression of magma rather than top-down fragmentation that is sometimes inferred for vulcanian eruptions (Hawke et al., 1989; Head III & Wilson, 1979; Jawin et al., 2015), and constraints in later sections on the fragmentation depth rely on this assumption. The model is not time integrated, and therefore is not duration sensitive (i.e., the calculations are equally applicable to sustained or nonsustained eruptions). We briefly explore in later sections the effects that incorporating materials of various densities (such as nonjuvenile material) has on the model.
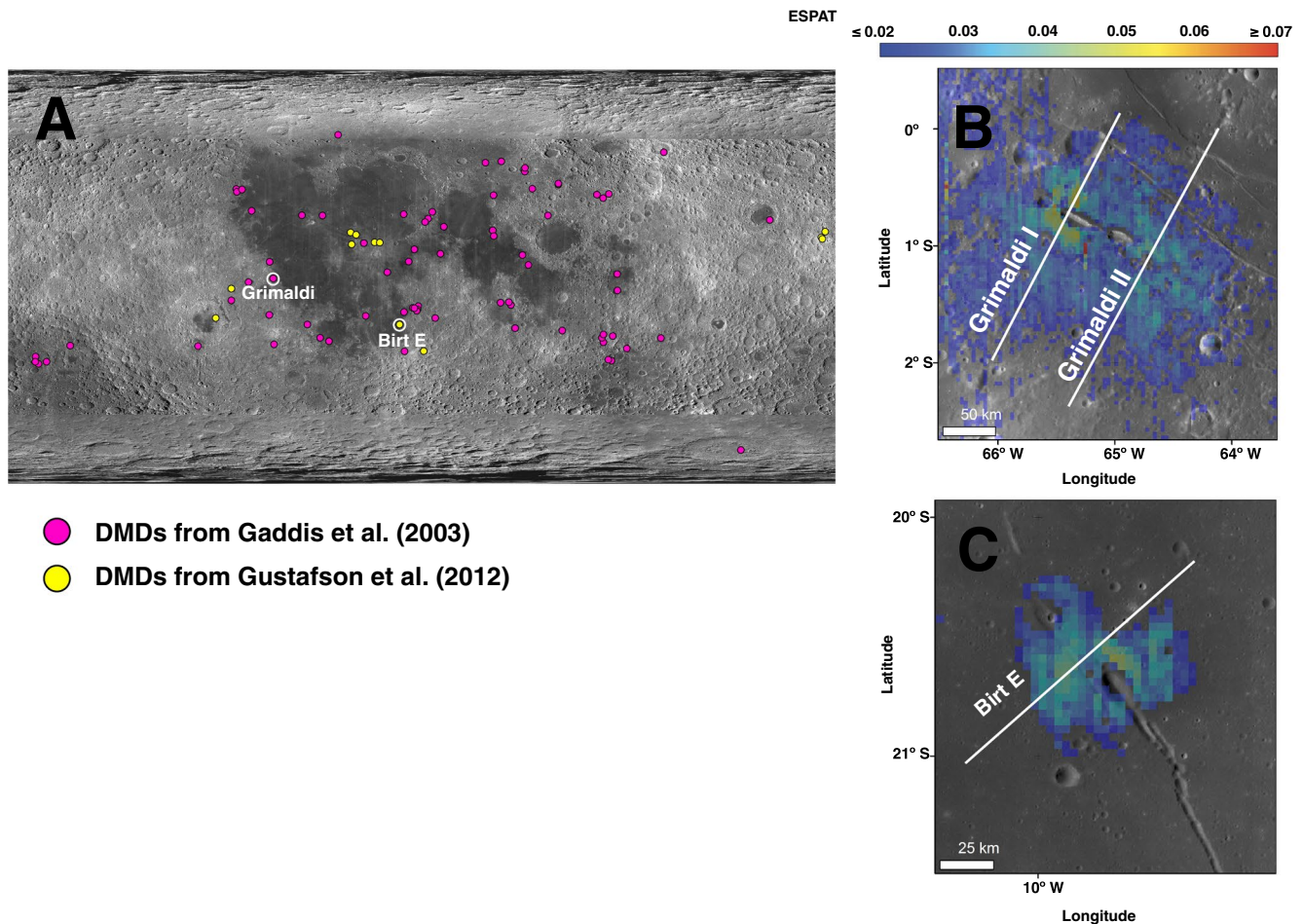
Figure 1. (a) Map of Dark-Mantle-Deposits (DMDs) in and around Procellarum Kreep Terrain identified from Gustafson et al. (2012) and Gaddis et al. (2003). DMDs Grimaldi and Birt E (investigated in this study) are circled in white. (b and c) ESPAT maps and approximate transect lines of DMDs Grimaldi and Birt E, respectively. ESPAT, Effective Single Particle Absorption Thickness.

The pyroclast sizes and water contents that are output by the model are used to predict the near-IR ESPAT values that would be observed in the M3 data (described in detail below), where the ESPAT values are a quantitative measure of the OH/H_2O absorption strength near a wavelength of ~2.9 μm and whose derivation is described in Milliken and Li (2017) and Li and Milliken (2017). We use maps of ESPAT values previously published by Milliken and Li (2017) and Li and Milliken (2017) to extract transects of ESPAT values over two small DMDs with identifiable vents: Birt E and Grimaldi (Milliken & Li, 2017) (Figure 1). The eruption dynamics model solves for the depth of magma fragmentation, which depends on the exsolved volatile content of the magma rising to the surface, and the ballistic trajectory of n pyroclasts of a certain size (diameter) distribution and preeruptive water content. The volatile loss experienced by each of the n pyroclasts is calculated with a diffusion model calibrated on the data of Saal et al. (2008). This allows us to generate a map of pyroclast size and postdiffusion water content as function of distance from the vent and thus construct synthetic ESPAT value maps for the two DMDs. The free parameters in the model are the prefragmentation water content of the rising magma, the concentration of exsolved volatiles at fragmentation, and pyroclast size distribution. The misfit between the synthetic (modeled) and measured ESPAT values of the DMD's are calculated and a Markov-Chain Monte-Carlo is implemented in order to retrieve the parameters that result in the best models (i.e., the most probable model parameters). Although the actual areal extent and even the corresponding source vents of many lunar DMDs may be obscured by younger mare deposits (Head, 1974), the inversion is preformed such that the model fits the entire ESPAT transect, and thus makes no assumptions of the deposit size other than that it is smaller than the length of the transect itself. Using this technique, we can ascertain the most probable preeruptive water content, concentration

Table 1
Table Summarizing Symbols for Coefficients Used in Model Calculations

Symbol	Definition	Units
n_{H_2O}	Mass fraction of prefragmentation water	
n_{gas}	Mass fraction of exsolved volatiles at fragmentation	
μ	Mean pyroclast size	ϕ
σ	Pyroclast size standard deviation	ϕ
d	Diameter of pyroclast	m
$\bar{d}$	Average pyroclast size of deposit	m
R	Radius of pyroclast	m
Q_u	Universal gas constant, 8.314×10^3	J kmol^{-1} K^{-1}
ρ_l	Density of picritic magma	kg/m^3
m	Molar mass of exsolved gas at fragmentation	kg/kmol
T_m	Temperature of melt	K
P_{frag}	Fragmentation pressure	Pa
P_{ch}	Choked flow pressure at vent	Pa
U_v	Vent velocity of gas and perfectly coupled pyroclasts	m/s
P_f	Final pressure gas expands to	Pa
N_a	Avogadro's number	mol^{-1}
ϕ_{gas}	Effective gas molecule diameter, $\sim 3.4 \times 10^{-10}$	m
U_f	Velocity of gas and perfectly coupled particles at P_f	m/s
u_t	Terminal velocity of pyroclasts	m/s
U_b	Initial ballistic velocities for pyroclasts	m/s
X	Dimension of thermally opaque gas cloud	m
R_f	Maximum range for pyroclastic deposit	m
F_e	Erupted volume flux of magma from fissure vent	m^3/s
t_{dike}	Total time pyroclasts spend in dike postfragmentation	s
t_{cloud}	Total time pyroclasts spend in gas cloud postdike	s
t_{total}	Total time pyroclasts spend diffusing	s
C^i	Concentration of volatile species i	ppm
β^i	Evaporation rate for chemical species i	m/s
D^i	Temperature dependent diffusivity for chemical species i	m^2/s
$D_o{}^i$	Diffusion coefficient for chemical species i	m^2/s

of exsolved gas upon fragmentation, as well as pyroclast size distribution parameters that reproduce the observed water absorption strengths (ESPAT values) for the deposits of interest. Definitions for all variables used by the model are provided in Table 1.

2.1. Eruption Model

We simulate the eruption and deposition of n pyroclasts using the eruption model of Wilson et al., (2010), Wilson and Keil (2012), Wilson and Head III (2003), Wilson and Head (2017), and Head and Wilson (2017), with model parameters **m**. Here, **m** can be written as:

$$\boldsymbol{m} = \left[n_{H_2O}, n_{gas}, \mu, \sigma \right] \tag{1}$$

Table 2
Table Summarizing all of the MCMC Runs Performed in This Study

Run #	DMD	n_{gas} (ppm)	n_{H_2O} (ppm)	σ (phi)	μ (Φ)/d_{50} (μm)	β (m/s)	Cooling rate (°C/s)
1	Grimaldi II	9932 ± 308	412 ± 18	0.46	0.76/410	1.4×10^{-6}	6.4
2	Grimaldi II	15025 ± 1213	674 ± 103	0.35	0.36/626	3.5×10^{-5}	6.4
3	Grimaldi II	9745 ± 614	400 ± 16	0.55	0.71/372	1.4×10^{-6}	6.4
4	Grimaldi II	13342 ± 1154	585 ± 50	0.34	0.47/575	3.5×10^{-5}	0.1
5	Grimaldi II	14314 ± 1322	773 ± 135	0.38	0.46/573	1.4×10^{-6}	0.1
6	Grimaldi II	6696 ± 395	246 ± 16	0.81	0.31/306	1.4×10^{-6}	6.4
7	Grimaldi II	7290 ± 224	266 ± 10	1.06	−1.10/310	1.4×10^{-6}	0.1
8	Grimaldi II	12612 ± 1264	507 ± 53	0.38	0.48/565	3.5×10^{-5}	6.4
9	Grimaldi II	13032 ± 887	580 ± 37	0.40	0.5/530	3.5×10^{-5}	0.1
10	Grimaldi I	29038 ± 1788	805 ± 152	0.79	−1.87/1,439	1.4×10^{-6}	0.1
11	Grimaldi I	52304 ± 1896	1317 ± 244	0.20	−1.04/1,865	3.5×10^{-5}	0.1
12	Grimaldi I	11167 ± 789	681 ± 63	1.03	−1.29/545	1.4×10^{-6}	6.4
13	Grimaldi I	21480 ± 1535	1151 ± 127	0.96	−2.1/1,058	3.5×10^{-5}	6.4
14	Grimaldi I	7226 ± 33938	497 ± 118	1.12	−1.5/473	1.4×10^{-6}	0.1
15	Grimaldi I	23291 ± 1774	1138 ± 576	0.8	−1.6/1,179	3.5×10^{-5}	0.1
16	Grimaldi I	6891 ± 409	474 ± 35	1.13	−1.59/1,495	1.4×10^{-6}	6.4
17	Grimaldi I	19490 ± 983	1055 ± 103	0.92	−2.09/1,265	3.5×10^{-5}	6.4
18	Birt E	5490 ± 856	505 ± 58	0.62	0.34/1,265	1.4×10^{-6}	0.1
19	Birt E	6998 ± 58	910 ± 48	1.77	−2.33/53	3.5×10^{-5}	0.1
20	Birt E	4642 ± 371	459 ± 54	0.47	1.26/291	1.4×10^{-6}	6.4
21	Birt E	12076 ± 1317	962 ± 197	0.18	0.36/713	3.5×10^{-5}	6.4
22	Birt E	4649 ± 256	420 ± 47	0.72	0.38/363	1.4×10^{-6}	0.1
23	Birt E	6959 ± 400	982 ± 102	0.82	0.96/195	3.5×10^{-5}	6.4
24	Birt E	4776 ± 552	448 ± 51	0.69	0.45/356	1.4×10^{-6}	6.4
25	Birt E	7168 ± 454	1188 ± 143	0.76	0.93/214	3.5×10^{-5}	0.1

Bolded run numbers indicate simulations run in the presence of a thermally opaque gas cloud. The parameters listed indicate the values that result in the best fit for each run. Table including the seeds for each run is included in the supporting information.

where n_{H_2O} is the initial concentration of dissolved H_2O in DMD parental magma upon fragmentation, n_{gas} is the concentration of the mixture of exsolved gas (CO, H_2O, S_2, SO_2, H_2S, and F) driving the eruption upon fragmentation (Rutherford et al., 2017), and μ and σ are the mean and standard deviation of the pyroclast size distribution. Here μ and σ are expressed in terms of Φ, where Φ is related to pyroclast size diameter, d, in mm as (Krumbein, 1934; Mueller et al., 2019):

$$d = 2^{-\Phi} \tag{2}$$

Using a lognormal relationship between Φ and wt % as implemented by Mueller et al. (2019), we generate a pyroclast size distribution for n pyroclasts (n = 40,000 for simulations presented in Table 2). Given pyroclast size parameters μ and σ, representing the mean and standard deviation of the deposit in terms of Φ, the fraction of the arbitrary population that any given pyroclast size comprises and the resulting average pyroclast size can be calculated, assuming that the density of the pyroclasts is constant and that the clasts do not contain any crystals.

The composition of the gas mixture exsolved from lunar picritic magmas upon fragmentation are best constrained using melt inclusion and glass data, as well as solubility experiments performed on orange

(high-Ti) lunar glass beads (Fogel & Rutherford, 1995; Rutherford et al., 2017; Wetzel et al., 2015, 2013). These studies suggest that the orange picritic glasses fragmented at a depth of 300–600 m, based on considerations of the concentration of C dissolved in melt inclusions, and that lunar eruptions are largely driven by exsolved C-species (Rutherford et al., 2017). Melt inclusion data from these studies, however, also suggest that presence of other exsolved volatile species contribute to the energy budget imparted unto pyroclasts at fragmentation (Rutherford et al., 2017). Because of this, n_{gas} represents the concentration of all exsolved gas species at fragmentation, including C-bearing species. Taking this into account, we use the composition of the exsolved gas phase of the picritic magma at depths of 300–600 m, as calculated by Rutherford et al. (2017) corresponding to 115 ppm CO, 10 ppm H_2O, 18 ppm S_2, 34 ppm SO_2, 19 ppm H_2S, and 10 ppm F, to calculate the molar mass of the exsolved volatile phase necessary to perform the model calculations involving n_{gas}. We briefly explore in later sections the sensitivity of the model calculations with respect to the molar mass of the exsolved volatile phase upon fragmentation, and therefore the composition.

To solve for the pyroclasts' trajectory, we first calculate the pressure (and depth) at which the rising magma is disrupted and transitions from a melt with suspended gas into a gas with suspended melt droplets by assuming a critical volume fraction of gas as 0.85 using the ideal gas law:

$$P_{frag} = \frac{0.15 \, n_{gas} \, Q_u \, T_m \, \rho_l}{0.85 \left(1 - n_{gas}\right) m} \tag{3}$$

where P_{frag} is the disruption pressure, n_{gas} is the mass fraction of exsolved volatiles, Q_u is the universal gas constant (8.314 kJ kmol^{-1} K^{-1}), T_m is the magmatic temperature, ρ_l is the density of the liquid phase, and m is the molar mass of the volatile mixture (Wilson & Head, 2017). The magmatic temperature here is assumed to be 1,450°C, slightly above the maximum liquidus of the green picritic glasses which ranges from 1,405 to 1,448°C (Delano, 1990). This assumption is supported by the fact that most picritic glasses tend to be crystal poor (Elkins-Tanton et al., 2003).

The pyroclasts are assumed to be perfectly coupled to the gas and therefore travel and accelerate with the gas as it expands to the choked flow conditions at the vent, P_{ch}, which can be calculated iteratively as Wilson and Head (2017):

$$\frac{n_{gas} \, Q_u \, T_m}{m} \ln \frac{P_{frag}}{P_{new}} + \frac{1 - n_{gas}}{\rho_l} \left(P_{frag} - P_{old}\right) = P_{old}^2 \frac{m}{2 \, n_{gas} \, Q_u \, T_m} \left(\frac{n_{gas} \, Q_u \, T_m}{m \, P_{old}} + \frac{1 - n_{gas}}{\rho_l}\right)^2 \tag{4}$$

With knowledge of the pressure of disruption and the pressure at the vent from Equation 4, the total time that the newly formed pyroclasts spend at high temperatures while being transported in the dike/conduit, t_{dike}, can be calculated using the Simpson integration rule (Atkinson, 1989) and integrating from the fragmentation depth to the surface.

From P_{ch} obtained from Equation 4, the averaged vent velocity, U_v, can be approximated as:

$$0.5 \, U_v^2 = \frac{n_{gas} \, Q_u \, T_m}{m} \ln \frac{P_{frag}}{P_{ch}} + \frac{1 - n_{gas}}{\rho_l} \left(P_{frag} - P_{ch}\right) - \left(\frac{P_{frag} - P_{ch}}{\rho_c}\right) \tag{5}$$

using the arguments from Wilson (1980) and Wilson and Head (2017), where ρ_c is the density of the lunar crust, 2,550 kg m^{-3} (Wieczorek et al., 2013). Next, the final pressure, P_f, at which the gas expands to outside of the vent can be calculated using Equation 6, which depends on the average pyroclast size of the eruption (Wilson & Head, 2017; Wilson et al., 2010). Pyroclasts that are perfectly coupled will inherit the velocity of the gas as it expands to P_f, where P_f is calculated as (Wilson & Head, 2017; Wilson et al., 2010):

$$P_f = \frac{2^{0.5} \, Q_u \, T_m}{3 \, \pi \, \varphi^2 \, N_a \, \bar{d}} \tag{6}$$
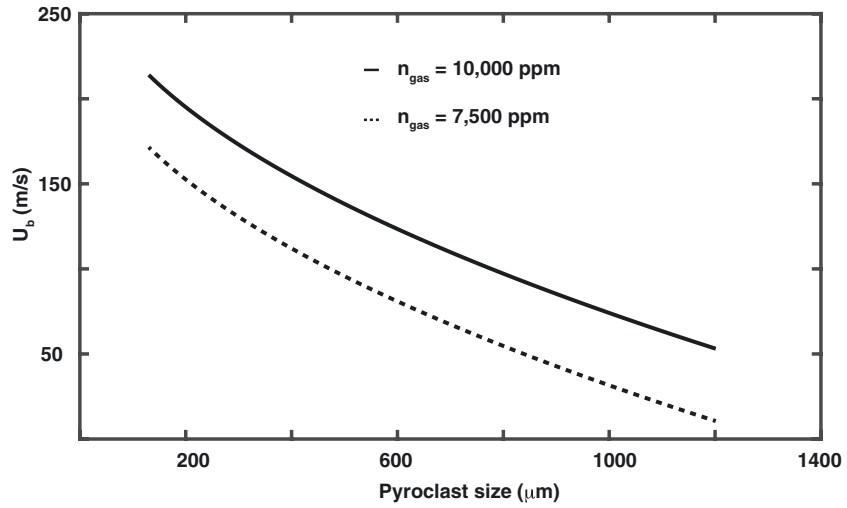
Figure 2. Schematic Initial ballistic velocities for pyroclasts, U_b, as a function of pyroclast size in diameter. The contours illustrate the dependence of U_b as a function of the concentration of exsolved volatiles upon fragmentation, n_{gas}.

where φ is the effective diameter of the gas molecules, 3.4×10^{-10} m for CO, $\bar{d}$ is the average pyroclast size, and N_a is Avogadro's number, 6.0225×10^{26} kmol^{-1}. At this point the expanding gas reaches a velocity of, U_f, calculated as (Wilson & Head, 2017):

$$0.5\,U_f^2 = 0.5\,U_v^2 + \frac{n_{\text{gas}}\,Q_u\,T_m}{m}\ln\frac{P_{\text{ch}}}{P_f} + \frac{1 - n_{\text{gas}}}{\rho_l}\Big[P_{\text{ch}} - P_f\Big] \tag{7}$$

The terminal velocity, u_t, by which the pyroclasts lags behind the expanding gas due to drag is calculated as (Wilson et al., 2010):

$$u_t = \left(\frac{4\,d\,\rho_c\,g}{3\,C_d\,\rho_g}\right)^{0.5} \tag{8}$$

where the Reynolds number is assumed to be large enough to be turbulent. Therefore, the initial ballistic velocity of each bead, U_b, can be calculated as:

$$U_b = U_f - u_t \tag{9}$$

From this point, the pyroclasts experience uninterrupted ballistic trajectory until deposition (Figure 2). Under conditions that may allow for an opaque gas cloud to form at the vent and thermally insulate the pyroclast, we compute the extent of that opaque cloud, X, from the maximum range of the pyroclasts following the treatment of Wilson and Keil (2012) for a fissure-like vent:

$$X = R_f - \frac{6.17\,\bar{d}\,R_f^{2.5}}{F_e} \tag{10}$$

The fissure-like geometry is assumed here to most closely reflect the shape of the inferred vents of the DMDs investigated in this study (Figure 1). From the extent of the opaque gas cloud, the time each pyroclasts spent in the hot gas cloud, t_{cloud}, can be calculated and added to the time each pyroclast spends traveling in the dike postfragmentation, t_{dike}, to compute the total time that each pyroclast spends above the closing temperature and experiences volatile loss by diffusion

$$t_{\text{total}} = t_{\text{dike}} + t_{\text{cloud}} \tag{11}$$

2.2. Diffusion Model

To determine the fraction of water remaining in each pyroclast after being deposited, we solve for the core-to-rim diffusion of water in a glassy sphere with evaporation at the surface according to the diffusion equation (Crank, 1975):

$$\frac{\partial C}{\partial t} = \frac{D(T)}{r^2} \frac{\partial}{\partial r}\left(r^2 \frac{\partial C}{\partial r}\right) \tag{12}$$

$$\frac{\partial C}{\partial r}\bigg|_{r=R} = \frac{-\beta}{D(T)}\left(C - C_o\right) \tag{13}$$

using an implicit, centered-space, finite-difference approximation. Further details of the discretization can be found in the supporting information. The inputs to this diffusion model are the total time of diffusion, t_{total}, the size of the pyroclast, d, and the prefragmentation water content, n_{H_2O} (Crank, 1975).

The size of any given pyroclast is determined from the pyroclast size distribution parameters σ and μ and the initial concentration of water is determined by the value n_{H_2O}, which are all left as free parameters. The total time of diffusion is determined by the time each pyroclast spends traveling in the opaque gas cloud. In this setup, the diffusion clock for each pyroclast therefore starts at fragmentation and ends at quenching: either after exiting the dike or exiting the gas cloud, depending on the presence or absence of gas cloud. The time each pyroclast spends traveling in the opaque gas cloud depends on the velocity of the pyroclast, the ballistic angle (trajectory), and therefore the pyroclast size, as well as the dimensions of gas cloud (determined by concentration of exsolved volatiles, n_{gas}, at fragmentation). n_{H_2O} is assumed to be constant throughout the pyroclasts at the onset of fragmentation and the pyroclasts are assumed to be completely glassy spheres, for simplicity. However, the evaporation rate, β, and the rate of cooling remain unconstrained and are necessary to calculate water loss.

To constrain these parameters, we expand upon the work of Saal et al. (2008) and determine the range of evaporation and cooling rates that give satisfactory fits to the core-to-rim volatile profiles of H_2O, F, Cl, and S, normalized for convenience, measured in several lunar pyroclastic glass beads. Although the source conditions and volatile content of the parental magma for the pyroclastic glass beads may be quite different from that of the parental magmas of Birt E and Grimaldi, the process and lunar environment which control volatile loss during pyroclast transport are likely similar, and therefore provide useful constraints on evaporation and cooling rates. These calculations are made simultaneously for all four species and we use a Markov-Chain Monte-Carlo approach to find the optimal set of evaporation and cooling rates that satisfy these profiles (see supporting information). The diffusion coefficients and activation energies used in the inversion are identical to those used in Saal et al. (2008) and are reported in Watson and Bender (1980) for Cl, Zhang and Stolper (1991) for H_2O, and Dingwell and Scarfe (1984) for F. For S, we use the assumption made in Saal et al. (2008) that the sulfur partitions primarily as S^2 at low f_{O_2} (Baker & Rutherford, 1996) and that the activation energy should be similar to that of O^{2-} reported in Wendlandt (1991). Finally, the diffusion coefficient for S is taken to be that reported in Saal et al. (2008). The choice for the diffusion coefficient of H_2O is likely not entirely accurate given that the value depends on the f_{O_2}. However, it is not well constrained for lunar magmas and therefore the value from Zhang and Stolper (1991) is chosen, following the treatment of Saal et al. (2008). Figure 3 shows an example of concentration profiles obtained with MCMC using this method and the range of admissible solutions after convergence (sampling the posterior distribution).

With these calculations, we can determine the upper and lower bounds of percent water loss: an upper limit using the highest H_2O evaporation rate and lowest cooling rate that provide satisfactory fits, and a lower bound by using the lowest H_2O evaporation rate and highest cooling rate that provided satisfactory fits. It is not entirely clear how formation and emplacement processes of the green picritic glasses, from which the diffusion constraints are obtained, relate to inferred pyroclasts at DMDs which we attempt to model. However, the DMDs are believed to be picritic as well, and the conditions for volatile diffusion and surface evaporation are presumed to be similar.
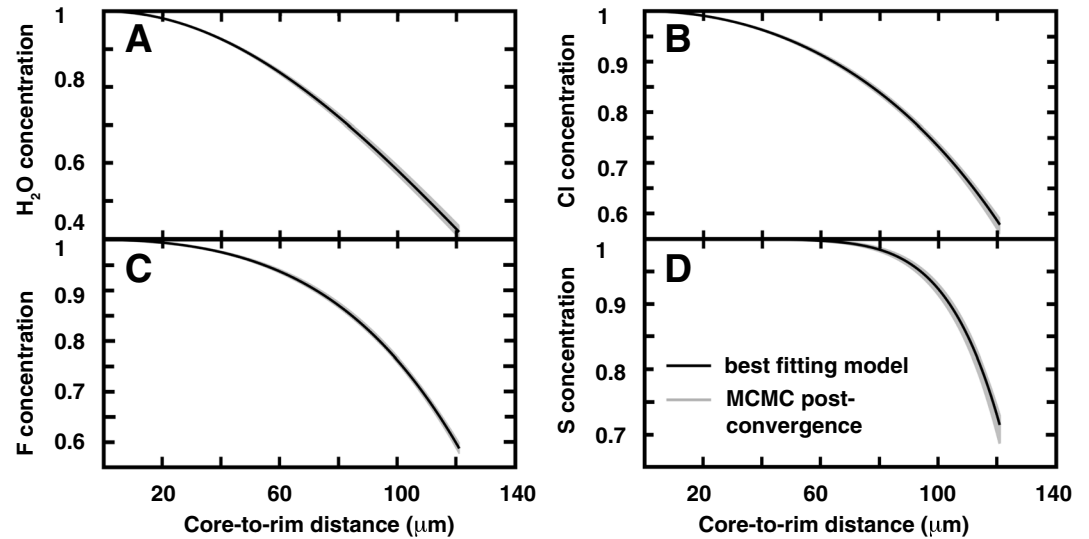
Figure 3. Diffusion plots with the normalized concentration of (a) H_2O, (b) chlorine, (c) fluorine, and (d) sulfur. As a function of core-to-rim distance within Delano's green glass bead #5 (very low-Ti). Bold black lines represent the best solution upon convergence of MCMC. Shaded gray areas represent the model output after convergence for a given MCMC run. MCMC, Markov-Chain Monte-Carlo.

Combining the eruption model outputs with the volatile diffusion and loss model results, we then calculate values of water content and pyroclast size with distance from the vent of the two DMDs. The size and water content of pyroclasts distributed radially away from the vent can then be converted to ESPAT values in two steps. First, we can calculate the particle size effect on ESPAT with values using the results of (Li & Milliken, 2017; Milliken & Mustard, 2005, 2007b):

$$slope = 0.6608 + 4.7067 \, exp\left(-0.04352 \, d\right) \tag{14}$$

where *slope* refers to the slope of the linear relationship between ESPAT values and water content, which varies with particle size. The ESPAT values are then calculated based on the water content from the eruption and diffusion model (Li & Milliken, 2016; 2017; Milliken & Li, 2017; Milliken & Mustard, 2007b):

$$\text{ESPAT} = \frac{1}{slope} \, \text{wt\%} \; H_2O \tag{15}$$

This approach is, in effect, a forward model of the near-IR water absorption strength based on the absorption path length (particle size) and concentration of the absorbing species (water content). The modeled ESPAT values can then be compared with the actual ESPAT value profiles from the M3 data and the parameters in the eruption model that result in the best fit can be determined. A schematic summary of the eruption-diffusion model is provided below in Figure 4.

2.3. Markov-Chain Monte-Carlo Inversion

The section above describes the flow chart to run (forward) a realization of a synthetic ESPAT profile away from a vent. The next step is to develop a nonlinear optimization scheme to find the free parameters, **m**

$$m = \left[n_{H_2O}, n_{gas}, \mu, \sigma \right] \tag{16}$$
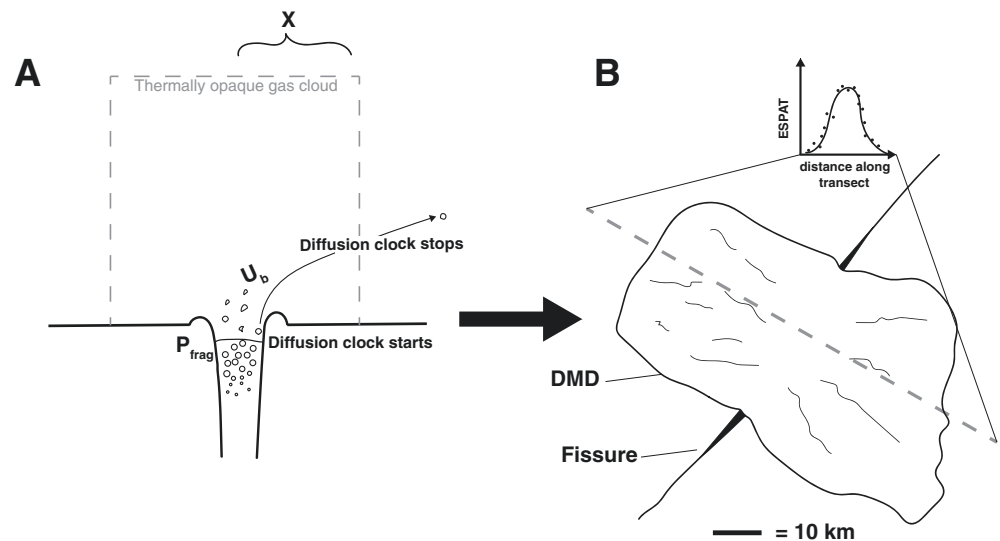
Figure 4. Schematic rendering of the eruption-diffusion model. (a) Schematic of critical stages of eruption model and (b) schematic of resulting numerical ESPAT that results from the simulated eruption. ESPAT, Effective Single Particle Absorption Thickness.

that minimize the residual between the numerically simulated ESPAT profile and that of the measured DMD. The optimization is performed with a Markov-Chain Monte-Carlo (MCMC) method. The MCMC is an inversion technique for nonlinear problems and allows sampling of the posterior distribution of the model parameters of interest (Anderson & Segall, 2013). The chain samples the posterior distribution by perturbing the model parameter vector **m** by a random amount in order to obtain **m′**. In this way, the future state of the chain obeys a Markovian process and depends only on the present state of the process when using the MCMC (Anderson & Segall, 2013). From **m′**, the forward eruption and water loss models are run and the ESPAT of the resulting deposit is calculated. If the residual is lowered between successive iterations, the new model parameters **m′** are saved and replace **m** for the next iteration. If the residual (L2-norm of the difference between observed and modeled ESPAT profiles) is not lowered, we compute the difference in likelihood between the solutions of the two consecutive iterations and use it to calculate the probability that the parameters of the last iteration are accepted. This finite probability allows a candidate vector, **m′**, that may fail to lower the residual to still be accepted and allow the model to escape local extrema (Anderson & Segall, 2013). This sequence is repeated for N iterations until the posterior distribution has been adequately sampled (in this study $N \sim 20{,}000$–$40{,}000$ iterations are sufficient to draw good statistics from the posteriori distributions).

3. Results

In order to obtain the upper and lower bounds of each parameter of the coupled eruption-water diffusion model, we explore the following scenarios: pyroclast diffusion calculations with boundary conditions that enhance water loss (corresponding to an evaporation rate of 3.5×10^{-5} m/s and a cooling rate of 0.1°C/s), as well as boundary conditions that limit water loss (corresponding to an evaporation rate of 1.4×10^{-6} m/s and a cooling rate of 6.4°C/s). These bounds are obtained from fitting diffusion profiles in the Apollo 15 green glasses measured by Saal et al. (2008). Intermediate combinations of these boundary conditions are also explored and tabulated in Table 2. The two DMDs investigated are Grimaldi, for which two ESPAT transects were evaluated (Grimaldi I and Grimaldi II), and Birt E. The measured ESPAT profiles for Grimaldi II are left unaltered, but some of the ESPAT values measured in the transects Grimaldi I and Birt E are not taken into account when calculating the misfit during the MCMC. Further details and justification about this omission can be found in section 4. The modeled ESPAT profiles agree closely with ESPAT transects of the two DMDs (Figures 5 and 7). Parameters converged upon by the MCMC are summarized in Table 2. Trace
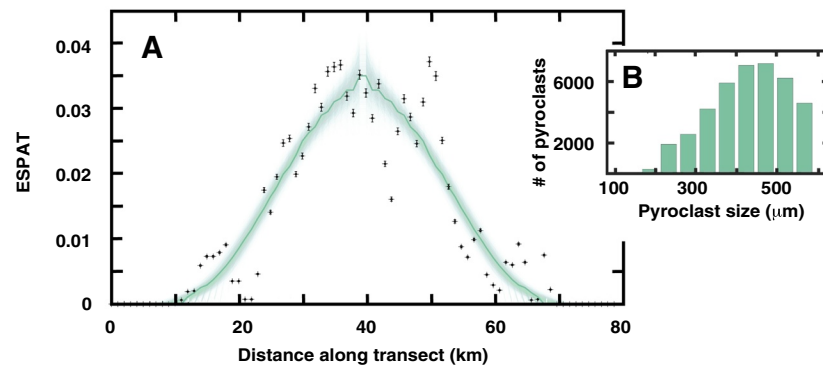
Figure 5. (a) The solid line represents the best fitting model for the second transect for the DMD Grimaldi II for an MCMC run of 10,000 iterations and an evaporation rate of 1.4×10^{-6} m/s and a cooling rate of 6.4°C/s. The green shaded area brackets the resulting ESPAT profiles sampled after the burn-in period (~1,000 iterations). (b) The resulting pyroclast size distribution for the best fitting model. DMD, Dark-Mantle-Deposit; MCMC, Markov-Chain Monte-Carlo; ESPAT, Effective Single Particle Absorption Thickness.

and covariate plots for different MCMC runs suggest convergence, with a burn-in period of ~1,000–2,000 iterations, depending on the initial seeds of the Markov-Chain Figure 6.

3.1. n_{H_2O}

Across all best fitting models for all of the DMDs, modeled with and without a thermally opaque gas cloud, best fitting models retrieve n_{H_2O} values that exhibit a total range from 246 ± 16 ppm to $1,317 \pm 244$ ppm. The error bounds are calculated as the standard deviation of the parameter's posteriori distribution sampled by the MCMC across the entire simulation after burn-in.

The best-fit solutions for Grimaldi I correspond to n_{H_2O} values that range from 681 ± 63 ppm to 1317 ± 244 ppm when accounting for a thermally opaque gas cloud during the eruption compared to the range from 474 ± 35 ppm to 1138 ± 576 ppm in the absence of a thermally opaque gas cloud. The lower and upper bound values for both cases are obtained with the least and most efficient water loss diffusion scenarios, respectively. Comparatively, the n_{H_2O} values of best fitting models for Grimaldi II return ranges from 400 ± 16 ppm to 773 ± 135 ppm (with gas cloud) and from 246 ± 16 ppm to 580 ± 37 ppm (without gas cloud). Finally, for Birt E, the best solution yields n_{H_2O} values that range from 459 ± 54 ppm to 962 ± 197 ppm (with gas cloud) and from 420 ± 47 ppm to 1188 ± 143 ppm (without gas cloud). Additionally, for each DMD, we see that the returned prefragmentation concentrations of water, n_{H_2O}, consistently increase as evaporation rate increases and cooling rate decreases (Table 2). For all of the DMDs, all else equal, the presence of a thermally opaque gas cloud results in higher prefragmentation water content (n_{H_2O} values).

3.2. n_{gas}

Best fitting models for all of the DMDs, both with and without a thermally opaque gas cloud, return corresponding n_{gas} values that exhibit a range from 4642 ± 371 ppm to 52304 ± 1896 ppm. The range of n_{gas} values for each individual DMD both with and without a thermally opaque gas cloud can be found in Table 2.

For each DMD, we see that the returned exsolved gas concentration upon fragmentation, n_{gas}, are also positively correlated with the inferred evaporation rate and negatively correlated with the cooling rate (Table 2). For the range of n_{gas} values returned, the corresponding confining pressure at the level of fragmentation range from ~1 to 11 MPa. The lower end of this range corresponds to models run for the less extensive Birt E deposit (~39 km transect) considering low evaporation rates and high cooling rates, whereas the higher end corresponds to the longer Grimaldi I transect (~85 km) and an assumption of high evaporation rates and low cooling rates (Table 2). In all cases modeled, except for Birt E with an evaporation rate of
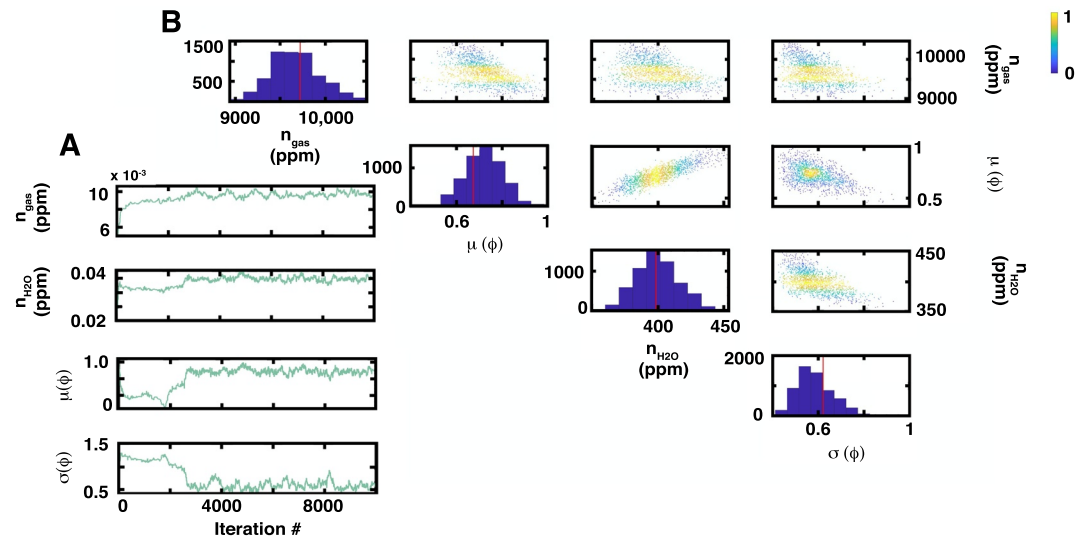
Figure 6. (a) Trace plots for MCMC run on Grimaldi II with an evaporation rate of 1.4×10^{-6} m/s and a cooling rate of 6.4°C/s. (b) Along diagonal of matrix of plots is the marginal posteriori distribution for each parameter with the solid red line representing the most likely solution in the parameter space, while the off-diagonal scatter plots highlight the covariance between parameters sampled from the posteriori distribution after burn-in. MCMC, Markov-Chain Monte-Carlo.

1.4×10^{-6} m/s and a cooling rate of 6.4°C/s, the presence of a thermally opaque gas cloud implies lower n_{gas} values (Table 2).

3.3. Pyroclast Size Distribution μ and σ

For convenience, pyroclast size distribution is discussed in terms of the best fitting models of pyroclast size in units of micrometers that corresponds to the 50th percentile of the size distribution, d_{50}. Across all best fitting models for all of the DMDs, modeled with and without a thermally opaque gas cloud, d_{50} ranges from 53 to 1,865 μm. The range of d_{50} values for each individual DMD both with and without a thermally opaque gas cloud can be found in Table 2. For each DMD, with few exceptions, the pyroclast size corresponding to the 50th percentile is positively correlated to evaporation rate and negatively correlated to cooling rate.

4. Discussion

Of the three DMD transects that were modeled, Grimaldi II exhibits a complete, continuous, and symmetric spatial ESPAT distribution, and thus offers the most robust constraints for the eruption-diffusion model (Figure 1). Asymmetry in the ESPAT maps and profiles (Figures 1 and 5) can be explained in several ways, including an angled conduit at the lunar surface, nonuniform topography, and uneven postemplacement modification or overlap of a younger unit. Additionally, Grimaldi I and Birt E both have ESPAT values of zero at the inferred vent, which is where one would expect ESPAT values to be highest as the largest pyroclasts are deposited near the vent and retain more water. Lower ESPAT values at or near the vent could possibly be explained by significant water loss for particles remaining within a thermally opaque cloud throughout the transport and perhaps even shortly after deposition. Alternatively, M3 pixels (spectra) directly over and adjacent to the vents can have low signal due to shadowing effects (e.g., see shadows for Birt E in Figure 1), which can result in falsely low values. Small-scale shadowing effects due to small impact craters and impact excavation of anhydrous material that lies beneath the DMD material may also explain some of the pixel-to-pixel variability in ESPAT values along the transects, such as some of the low points observed in Figure 7a for Grimaldi I. For simplicity, we omit these anomalous data points toward the center of the Grimaldi I and Birt E transects and focus instead on the tails of the ESPAT distribution away from the vent as they are more sensitive to eruption dynamics and pyroclast size distribution. Despite this omission, the range of values returned for each parameter for the three modeled ESPAT transects show
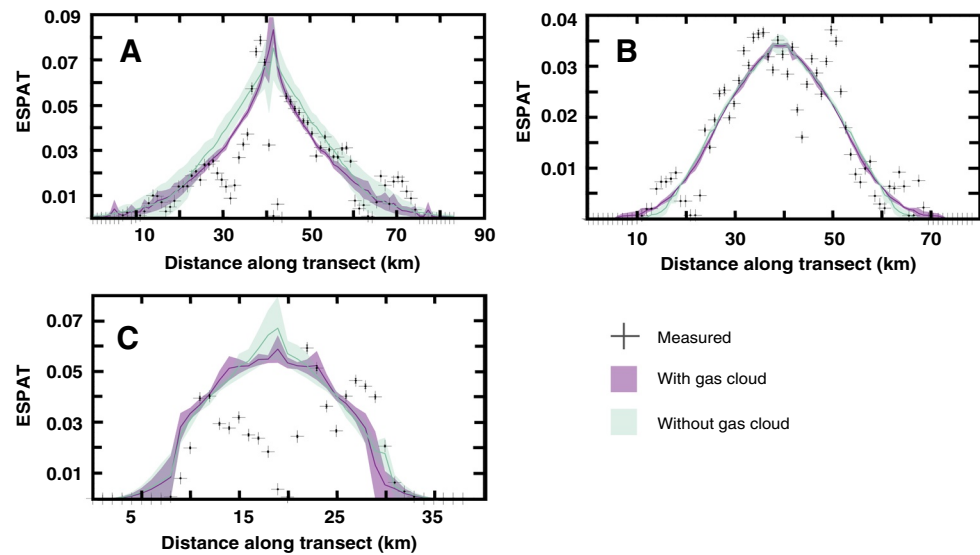
Figure 7. Best fitting models to the measured ESPAT profile for each combination of evaporation rate and cooling rate for (a) Grimaldi I, (b) Grimaldi II, and (c) Birt E. The solid line indicates the most likely solution, light shades indicate total range spanned by the posteriori distribution of the MCMC for inversions that include and neglect the presence of an opaque gas cloud. MCMC, Markov-Chain Monte-Carlo; ESPAT, Effective Single Particle Absorption Thickness.

significant overlap. To our knowledge, these results offer tighter constraints on these parameters for lunar pyroclastic eruptions and their parental magmas than previously offered (Hauri et al., 2011; Rutherford et al., 2017; Saal et al., 2008, 2013). Importantly, the results also demonstrate that reasonable values for these parameters can be achieved that both fit the remotely sensed near-IR data and are consistent with current pyroclastic eruption models.

4.1. n_{H_2O}

For a given ESPAT transect, as one considers a scenario that would enhance water loss (slower cooling rate or higher evaporation rate), the best fit model parameters are adjusted by increasing the amount of prefragmentation water such that the quality of the ESPAT profile fit is maintained (Table 2). A satisfactory fit can be found for each combination of evaporation and cooling rate applied to each transect, but the only overlap in solution space in terms of prefragmentation water content between all three DMD transects occurs in a narrow range from ~400 to 800 ppm (Figure 8b).

For Grimaldi, considering both transects, the range for prefragmentation water content likely ranges from ~400 to 800 ppm on the basis of the overlap in n_{H_2O} solution space both with and without gas cloud, or ~500–600 ppm if considering only the scenarios without a thermally opaque gas cloud (Figure 8b and Table 2). Because Grimaldi I and II were transects measured across the same DMD, the true prefragmentation water returned by the eruption-diffusion model should agree. With or without the presence of a thermally opaque gas cloud, the only models for both Grimaldi I and II that fall within or near this overlapping solution space are the scenario with an evaporation rate of 1.4×10^{-6} m/s and 6.4°C/s (Figure 8b and Table 2).

For Birt E, the best fitting models for the same evaporation rate of 1.4×10^{-6} m/s and cooling rates of either 0.1 and 6.4°C/s also return prefragmentation water concentrations consistent with that of Grimaldi, 400–800 ppm (Figure 8b and Table 2), while n_{H_2O} values for best fitting models with an evaporation rate of 3.5×10^{-5} m/s and either a cooling rate of 0.1 or 6.4°C/s yield higher values from 910 to 1,188 ppm. While the n_{H_2O} values returned for Birt E that were obtained assuming high evaporation rates could be explained by the presence of spatial heterogeneities in the distribution of water in DMD source material, the values for n_{H_2O} remain within the range modeled for Grimaldi I (Figure 8b and Table 2). Because of this, it is likely that the prefragmentation water content in these DMD are similar and that the evaporation rate during
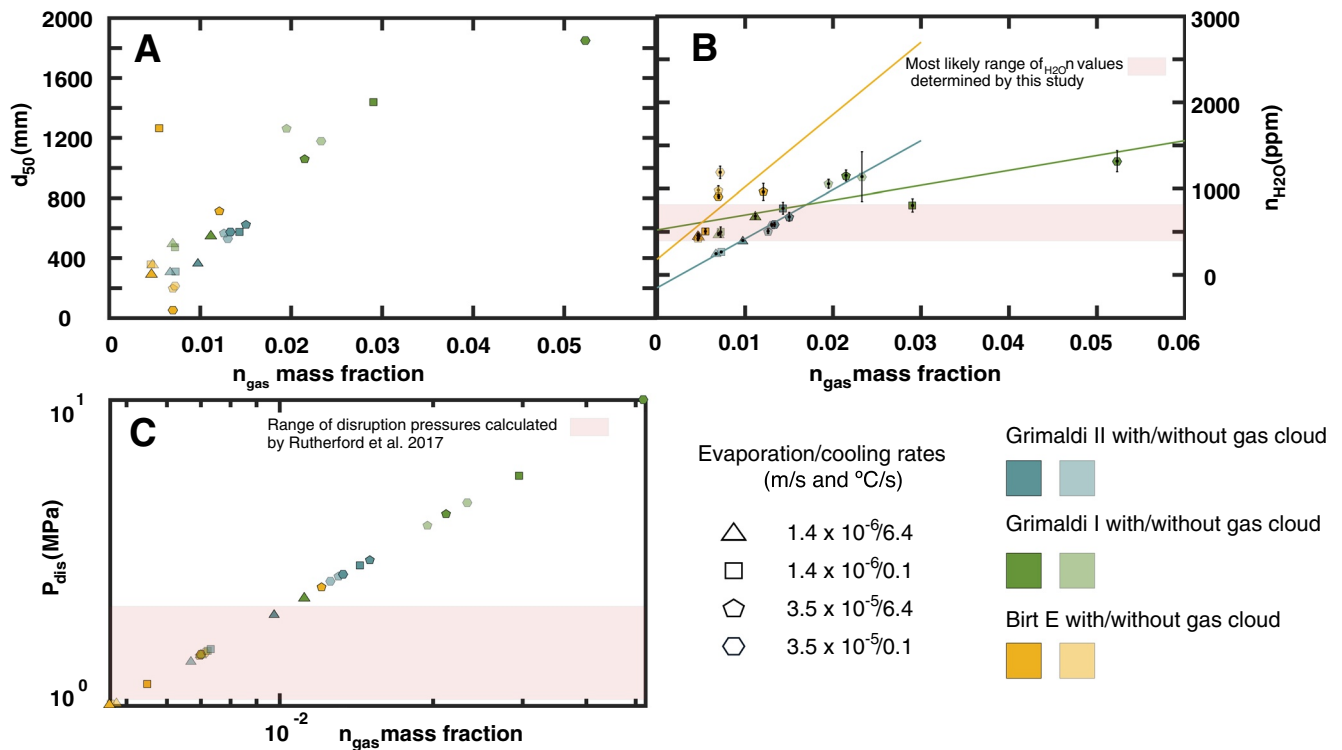
Figure 8. The parameters that resulted in the best fitting models for each MCMC run are plotted here. (a) Pyroclast size corresponding to the 50th percentile, (b) wt % H_2O prefragmentation, and (c) fragmentation pressure versus mass fraction of exsolved gas at fragmentation. The range highlighted in panel (c) corresponds to the range of fragmentation depths for the orange picritic glasses determined petrologically by Rutherford et al. (2017). MCMC, Markov-Chain Monte-Carlo.

lunar eruptions tends toward values closer to that of 1.4×10^{-6} m/s, at least for eruptions with a thermally opaque gas cloud.

4.1.1. Agreement of n_{H_2O} with Previous Petrologic Studies

The most likely range of water contents determined in this study (400–800 ppm) is in good agreement with the most likely range of water contents previous studies have reported for parts of the lunar interior sampled by the lunar picritic glasses (260–745 ppm; Saal et al., 2008, 615–1,410 ppm; Hauri et al. 2011). Our results support the growing body of work that suggests parts of lunar interior are more enriched in volatiles than previously thought (Hauri et al., 2011; Rutherford et al., 2017; Saal et al., 2008, 2013). In the absence of any constraints, the prefragmentation water content for the parental magmas of Birt E and Grimaldi inferred from this study span a range of 246–1317 ppm (Figure 8b and Table 2). These values are a lower bound as they do not take into account any water lost from outgassing prefragmentation. We note however, that the data from olivine melt inclusions in Apollo 17 orange glass beads suggest a very small H_2O fraction in the prefragmentation gas phase. Additionally, these values may not be representative of the bulk lunar mantle as the lunar glasses are believed to be generated from partial melting of differentiated and likely volatile enriched LMO material (Delano, 1986; Hess & Parmentier, 1995; Shearer et al., 2006), and the degree of partial melting is estimated to be 5%–10% (Saal, et al., 2008).

4.1.2. Agreement Distribution of Water in Lunar Pyroclastic Deposits Reported in Milliken and Li (2017)

The final distribution of water and average pyroclast diameter corresponding to each best fitting simulation with water loss calculated with evaporation and cooling rates of 1.4×10^{-6} m/s and 6.4°C/s, respectively, are reported in Figure 9. Milliken and Li (2017) assumed the DMDs investigated were spectrally dominated by particles (pyroclasts) ~60–80 μm in diameter in order to estimate the amount of water indigenous to the deposits. The results presented in this study instead solve for pyroclast size and find that the pyroclast
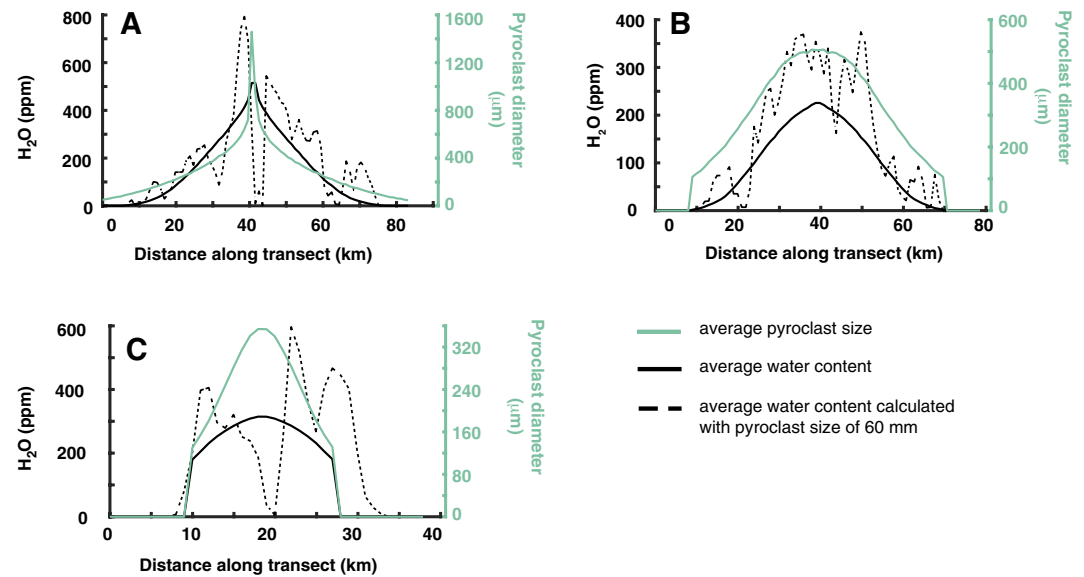
Figure 9. Average pyroclast diameter determined and postdeposition water content from best fitting models for (a) Grimaldi I, (b) Grimaldi II, and (c) Birt E, along with water contents calculated similar to those of Milliken and Li ([2017]) using fixed pyroclast diameter of 60 μm. Each of the best fitting models here are for evaporation and cooling rates of 1.4×10^{-6} m/s and 6.4°C/s, respectively.

size distributions that result in the best fitting models are on average larger than that used in Milliken and Li ([2017]), sometimes by an order of magnitude. This results in the current DMD water contents reported in Milliken and Li ([2017]) to be, on average, higher than the results presented in this work. Despite the large differences in pyroclast sizes (Figure 9), the differences in the final water contents of the DMDs is not huge and it is still clear that the DMDs are more hydrated than surrounding regions. Most importantly, the results described here demonstrate that there exist a suite of conditions for which the near-IR spectral data can be modeled and which are simultaneously consistent with current eruption models. The integration of the models and the remotely sensed data further support the notion that the magmas that gave rise to the DMDs are enriched in water.

4.1.3. n_{gas}

The exsolved gas concentration upon fragmentation, n_{gas}, exerts important controls over the model and, ultimately, the fit to the observed ESPAT data. The value of n_{gas} directly influences the depth of fragmentation, the size of the thermally opaque gas cloud (if any), the trajectories of the pyroclasts forming the deposit, and consequently the extent of water loss by degassing. As water loss is enhanced, the values of n_{gas} that result in the closest ESPAT fits tend to increase (Table 2). This is largely because at a fixed n_{gas}, the distribution of pyroclasts away from the vent remains identical but enhanced water loss decreases the calculated ESPAT values across the profile. To counteract this effect and retrieve an acceptable fit to observed ESPAT profiles, the solution space is shifted toward a larger pyroclast size distribution (i.e., if the concentration of the absorbing species decreases then the absorption path length must increase to maintain the same absorption strength). To enable the larger pyroclasts to travel the same distance, the n_{gas} must increase so that the pyroclasts inherit enough kinetic energy to match the extent of the observed water signature in the near-IR data.

4.1.4. Agreement of n_{gas} with Previous Petrologic Studies

For the range of n_{gas} values returned, the corresponding pressure at the fragmentation level ranges from ~1 to 11 MPa (Figure 8). Considering the Grimaldi models with overlapping solution space as well as all of the best fitting models for Birt E, this range reduces to ~1–3 MPa (Figure 8 and Table 2). This lower range is in close agreement with values determined from petrological studies using C dissolved in melt inclusions in picritic orange glasses that suggest fragmentation at ~1–2 MPa (Rutherford et al., [2017]), with our results corresponding to a range in n_{gas} of ~4,500–12,000 ppm. We reiterate that the composition of the exsolved gas at fragmentation used for the models is that reported by Rutherford et al., ([2017]), with a molar mass of 36 g/

mol. To investigate the dependence of our results on the composition of the exsolved gas, for the least efficient water loss conditions applied to Grimaldi II, two additional MCMCs were run: one with an arbitrary molar mass of exsolved gas of 20 g/mol and with 65 g/mol. Assuming a molar mass for the gas mixture of 65 g/mol, we find that the disruption pressure is decreased by less than 0.1 MPa and the prefragmentation water content reduced from 400 to 340 ppm. Using instead 20 g/mol, the disruption pressure is increased by ∼0.5 MPa and the prefragmentation water content is increased from 400 to 520 ppm. This range in possible molar masses for a given composition of exsolved gas represents extreme upper and lower bounds and seems to suggest that the composition does not significantly alter the results.

As determined by Rutherford et al. (2017) based on gas solubility experiments and analyses of the orange picritic glasses, the abundance of exsolved gas at the transition from equilibrium to kinetic degassing is too low to lead to magma fragmentation. Using C values measured in the orange picritic glass, Rutherford et al. (2017) estimate the depth of fragmentation to be within 300–600 m from the surface (1–2 MPa), and therefore determine that there is a contribution from open-system degassing. The concentration of exsolved volatiles at fragmentation returned by our models are in excess of those calculated by Rutherford et al. (2017) for closed-system degassing. The difference between the values of n_{gas} returned by our model and the closed-system degassing calculated by Rutherford et al. (2017) (∼200 ppm) represents the contributions from open-system degassing. The inability of closed-system degassing to cause fragmentation at depths that agree with those determined petrologically by Rutherford et al. (2017) in the orange picritic glasses as well as the large n_{gas} values determined in this study can at least in part be explained by the dike-tip propagation model of lunar glass formation proposed by Head and Wilson (2017). In this model, efficient open-system degassing allows a volatile-rich foam to form at the tip of a propagating dike and propels the orange picritic glass magma to the lunar surface.

4.1.5. Pyroclast Size Distribution μ and σ

The pyroclast size distribution affects the ballistic trajectory of the pyroclast, the loss of volatiles by diffusion, and also directly influences the modeled ESPAT values. This effect of pyroclast size on water loss can be seen as models trade-off between pyroclast size and the assumed conditions for water loss (evaporation and cooling rates). Models run under conditions that do not favor volatile retention (high evaporation rates and low cooling rates) return larger average pyroclast size distributions because larger pyroclasts retain water more readily than smaller pyroclasts (Figure 8 and Table 2). Furthermore, the lateral extent of the modeled deposits depends on the pyroclast size distribution because smaller pyroclasts inherit a greater proportion of the momentum of the expanding gas cloud, which explains the positive correlation between average pyroclast size and mass fraction exsolved gas at fragmentation.

Across all of the best models, the returned pyroclast size distributions are such that d_{50} ranges from 53 to 1,865 μm (Figure 8 and Table 2). When considering the added constraints for the fragmentation depth from Rutherford et al. (2017), this range reduces to 53 to 1,265 μm (Figure 8). For Grimaldi, when considering only the models with parameters that overlap for Grimaldi I and II, the range in pyroclast sizes is further reduced to 372–626 μm (Figure 8 and Table 2). For Birt E, the total range in pyroclast sizes (again 50th percentile) range from 53 to 1,265 μm for the best fitting models (Figure 8 and Table 2). Despite the large range in pyroclast sizes determined by the inversion calculation, the solutions with the highest likelihood agree with the observation that the picritic glasses are submillimeter (<1 mm) (Heiken et al., 1991; Rutherford et al., 2017; Saal et al., 2008).

4.1.6. Agreement of Pyroclast Size Distribution with Previous Petrologic Studies

The DMDs investigated in the present study are not related to the sites from which samples were returned by the Apollo and Luna missions. The returned picritic glass samples display a typical range of mean pyroclast size of 45–100 μm (Heiken et al., 1991; Rutherford et al., 2017). For the most probable best fitting models, those that agree with the fragmentation depth determined by Rutherford et al. (2017) as well as the models that provide agreement between the two ESPAT transects for Grimaldi, the pyroclast size corresponding to 50th percentile range from 372 to 1,265 μm. This is larger than the range of average pyroclast sizes observed in the Apollo soils (Heiken et al., 1991). The discrepancy can be attributed, at least in part, to the fact that samples at or near a known vent have not been acquired. Samples from this region would contain larger pyroclasts and potentially be less well-sorted.

4.1.7. Constraints on Evaporation and Cooling Rate

In addition to each of the parameters constrained by this work, we find that the combinations of evaporation rate and cooling rate that provide mutual satisfactory fits to the two Grimaldi transects only occur at low evaporation rates (10^{-6} m/s) (Figure 8b and Table 2), in agreement with the low evaporation rates determined experimentally by Arndt et al. (1984), and with the diffusion profiles modeled numerically by Saal et al. (2008). However, we find that only cooling rates slightly above the range determined by Saal et al. (2008) (<5°C/s) provide model results that agree between the two Grimaldi transects (6.4°C/s) (Figure 8b and Table 2). ESPAT values for the Birt E transect, however, can be adequately fit using any combination of evaporation rate (either 1.4×10^{-6} m/s or 3.5×10^{-5} m/s) and cooling rate (0.1 or 6.4°C/s). Moreover, all combinations for the water loss for Birt E provide reasonable fits within the fragmentation depth constraints of Rutherford et al. (2017) (fractionation depths of 300–500 m) (Figure 8 and Table 2).

4.1.8. Effects of Variations in Glass Content on Results

It is worth noting that, for simplicity, we assume that the density of the clasts is constant and that the clasts do not contain any crystals. While this assumption is accurate for entirely glassy deposits, estimates of the abundance of glass in Birt E and Grimaldi are 77 and 71 wt %, respectively (Trang et al., 2017). The average density of the deposit is expected to increase with increasing clinopyroxene abundance (18 and 20 wt % clinopyroxene for Birt E and Grimaldi, respectively (Trang et al., 2017)). To test the behavior of the eruption model in response to this average increase in density, we run an MCMC inversion identical to model run 3 (Table 2), except using a constant density of 3,200 kg/m³. The parameters that result in the best fit tend to shift to lower values compared to those calculated using a lower density. Using a density of 2,900 kg/m³ the returned n_{H_2O} is 400 ppm and d_{50} is 372 μm. Using a density of 3,200 kg/m³ the returned n_{H_2O} is 380 ppm and d_{50} is 324 μm. Results are similar for n_{gas}.

In addition to the effect on the average density and the kinetics of deposition, small amounts of crystallinity will also slow down volatile diffusion within the clasts by a few percent and can be accounted for by introducing a formation factor for diffusion (Huber & Su, 2015). This would likely have a similar effect as outlined in the paragraph above and result in slightly lower best fitting n_{H_2O} values. This is because the inhibition of volatile diffusion allows for smaller n_{H_2O} values to satisfy the residual water content of the deposit.

5. Conclusion

Constraining the lunar volatile budget is important to further our understanding of lunar formation and evolution as well as volcanic eruptions. Models of lunar formation and evolution must be able to explain the retention of volatiles in parts of the lunar interior (Hauri et al., 2011; Rutherford et al., 2017; Saal et al., 2008, 2013). The present study offers constraints on the prefragmentation water content of glasses forming two Dark-Mantle-Deposits (DMDs), Birt E and Grimaldi, where we can use spectral data (ESPAT values at near-IR wavelengths) to extract information about water content and pyroclast size.

Our results suggest that the most likely range in water content in the glass before fragmentation is 400–800 ppm, and that the lunar interior source regions for both Birt E and Grimaldi are not devolatilized and devoid of water. This is in agreement with the many studies investigating the dissolved volatile content of lunar magmas and their source regions by means of melt inclusions, picritic glasses, and lunar apatites.

The most probable range of prefragmentation water contents for the very-low-Ti glasses is 260–745 ppm according to Saal et al. (2008) and 615–1,410 ppm from Hauri et al. (2011). Our results are in close agreement with that of Saal et al. (2008), which provided the data from which evaporation and cooling rate constraints were obtained, and is only slightly lower than the range determined by Hauri et al. (2011). This is likely because Hauri et al. (2011) obtained the range in water content by analyzing dissolved water in melt inclusions, capturing the trend of decreasing H2O in trapped melt with decreasing pressure just prior to melt fragmentation.

The method used in this study not only provides tighter constraints on prefragmentation water contents, but it also provides constraints for the concentration of exsolved gas at fragmentation and constraints for the pyroclast size distribution of DMDs. The concentration of exsolved volatiles at fragmentation according to our best fitting models are in excess of the concentrations calculated by Rutherford et al. (2017) assuming closed-system degassing. This supports their conclusion that open-system degassing plays a significant role on the eruption dynamics of these fire-fountain eruptions and is in part explained by the dike formation model of Wilson and Head III (2003) and Head and Wilson (2017).

Furthermore, the results of our work offer constraints on the pyroclast size distribution of Birt E and Grimaldi as well as the conditions above the blocking temperature associated with the deposits. Our results suggest that the pyroclast size diameter corresponding to the 50th percentile, across both Grimaldi and Birt E, likely ranges from ~400 to 600 um, and that the evaporation and cooling rates are likely low, ~10^{-6} m/s and ~6°C/s, respectively.

The calculations for water loss use a range of evaporation and cooling rates obtained by fitting diffusion data for the very low-Ti lunar glasses. Therefore, an important assumption this model makes is that the diffusional environment for the pyroclasts associated with the DMDs being investigated is similar to the very low-Ti, green lunar glasses. Additionally, the constraints on fragmentation come from calculations made on the high-Ti, orange lunar glasses and may not be applicable to the DMDs investigated here. The orange glasses are believed to have a higher cooling rate than the other lunar glasses (Arndt et al., 1984; Arndt & Von Engelhardt, 1987), and if indeed the DMDs investigated here more closely represent the orange glasses, the prefragmentation water content, the exsolved gas concentration at fragmentation, and the mean pyroclast size returned by the best fitting models would likely decrease (Figure 8 and Table 2). Additional information on the titanium content of lunar DMDs could further constrain the results presented here.

This study suggests that in the absence of new samples returned from lunar DMDs, a combination of remote sensing, numerical modeling, and petrology can be used to determine the prefragmentation water content for different DMD magmas and make inferences about the volatile composition of their source material. The extent to which different parts of the lunar interior may exhibit heterogeneous amounts of volatiles may not be entirely determinable at present from the two DMDs investigated in this study, but the template presented here may help fill in those gaps.

Data Availability Statement

Codes are available and archived at the Brown Digital Repository, Brown University Library, https://doi.org/10.26300/8pmw-yw23.

References

Anderson, K., & Segall, P. (2013). Bayesian inversion of data from effusive volcanic eruptions using physics-based models: Application to Mount St. Helens 2004-2008. *Journal of Geophysical Research: Solid Earth*, *118*, 2017–2037. https://doi.org/10.1002/jgrb.50169

Arndt, J., Engelhardt, W. V., Gonzalez-Cabeza, I., & Meier, B. (1984). Formation of Apollo 15 green glass beads. *Journal of Geophysical Research*, *89*(S01), C225–C232. https://doi.org/10.1029/jb089is01p0c225

Arndt, J., & Von Engelhardt, W. (1987). Formation of Apollo 17 orange and black glass beads. *Journal of Geophysical Research*, *92*(B4), E372–E376. https://doi.org/10.1029/jb092ib04p0e372

Atkinson, K. E. (1989). *An introduction to numerical analysis*. New York, NY: John Wiley & Sons, Inc.

Baker, L. L., & Rutherford, M. J. (1996). Sulfur diffusion in rhyolite melts. *Contributions to Mineralogy and Petrology*, *123*(4), 335–344. https://doi.org/10.1007/s004100050160

Besse, S., Sunshine, J. M., & Gaddis, L. R. (2014). Volcanic glass signatures in spectroscopic survey of newly proposed lunar pyroclastic deposits. *Journal of Geophysical Research: Planets*, *119*, 355–372. https://doi.org/10.1002/2013JE004537

Boyce, J. W., Liu, Y., Rossman, G. R., Guan, Y., Eiler, J. M., Stolper, E. M., & Taylor, L. A. (2010). Lunar apatite with terrestrial volatile abundances. *Nature*, *466*(7305), 466–469.

Canup, R. M. (2004). Dynamics of lunar formation. *Annual Review of Astronomy and Astrophysics*, *42*, 441–475. https://doi.org/10.1146/annurev.astro.41.082201.113457

Crank, J. (1975). *The mathematics of diffusion*. New York, NY: Oxford University Press.

Delano, J. (1980). Chemistry and liquidus phase relations of Apollo 15 red glass Implications for the deep lunar interior. Paper presented at Lunar and Planetary. *Science Conference Proceedings*, Houston, TX.

Delano, J. (1990). Buoyancy-driven melt segregation in the earth's moon. I: Numerical results. Paper Presented at Lunar and Planetary. *Science Conference Proceedings,* Houston, TX.

Delano, J. W. (1986). Pristine lunar glasses: Criteria, data, and implications. *Journal of Geophysical Research*, *91*(B4), 201–213. https://doi.org/10.1029/jb091ib04p0d201

Delano, J. W., & Lindsley, D. H. (1983). Mare glasses from Apollo 17: Constraints on the Moon's bulk composition. *Journal of Geophysical Research*, *88*(S01), B3–B16. https://doi.org/10.1029/jb088is01p000b3

Dingwell, D. B., & Scarfe, C. M. (1984). Chemical diffusion of fluorine in jadeite melt at high pressure. *Geochimica et Cosmochimica Acta*, *48*(12), 2517–2525. https://doi.org/10.1016/0016-7037(84)90302-8

Elkins, L. T., Fernandes, V. A., Delano, J. W., & Grove, T. L. (2000). Origin of lunar ultramafic green glasses: Constraints from phase equilibrium studies. *Geochimica et Cosmochimica Acta*, *64*(13), 2339–2350. https://doi.org/10.1016/s0016-7037(00)00365-3

Elkins-Tanton, L. T., Chatterjee, N., & Grove, T. L. (2003). Experimental and petrological constraints on lunar differentiation from the Apollo 15 green picritic glasses. *Meteoritics & Planetary Science*, *38*(4), 515–527

Fogel, R. A., & Rutherford, M. J. (1995). Magmatic volatiles in primitive lunar glasses: I. FTIR and EPMA analyses of Apollo 15 green and yellow glasses and revision of the volatile-assisted fire-fountain theory. *Geochimica et Cosmochimica Acta*, *59*(1), 201–215. https://doi.org/10.1016/0016-7037(94)00377-x

Gaddis, L. R., Hawke, B. R., Robinson, M. S., & Coombs, C. (2000). Compositional analyses of small lunar pyroclastic deposits using Clementine multispectral data. *Journal of Geophysical Research*, *105*(E2), 4245–4262. https://doi.org/10.1029/1999JE001070

Gaddis, L., Rosanova, C., Hare, T., Hawke, B., Coombs, C. & Robinson, M. (1998). Small lunar pyroclastic deposits: A new global perspective. *Lunar and Planetary Science XXIX*, 1807.

Gaddis, L. R., Pieters, C. M., & Ray Hawke, B. (1985). Remote sensing of lunar pyroclastic mantling deposits. *Icarus*, *61*(3), 461–489. https://doi.org/10.1016/0019-1035(85)90136-8

Gaddis, L. R., Staid, M. I., Tyburczy, J. A., Hawke, B. R., & Petro, N. E. (2003). Compositional analyses of lunar pyroclastic deposits. *Icarus*, *161*(2), 262–280. https://doi.org/10.1016/s0019-1035(02)00036-2

Greenwood, J. P., Itoh, S., Sakamoto, N., Warren, P., Taylor, L., & Yurimoto, H. (2011). Hydrogen isotope ratios in lunar rocks indicate delivery of cometary water to the Moon. *Nature Geoscience*, *4*(2), 79–82. https://doi.org/10.1038/ngeo1050

Gustafson, J. O., Bell, J. F., Gaddis, L. R., Hawke, B. R., & Giguere, T. A. (2012). Characterization of previously unidentified lunar pyroclastic deposits using Lunar Reconnaissance Orbiter Camera data. *Journal of Geophysical Research: Planets*, *117*, E00H25. https://doi.org/10.1029/2011JE003893

Hapke, B. W., Nelson, R. M., & Smythe, W. D. (1993). The opposition effect of the moon: The contribution of coherent backscatter. *Science*, *260*(5107), 509–511. https://doi.org/10.1126/science.260.5107.509

Hauri, E. H., Weinreich, T., Saal, A. E., Rutherford, M. C., & Van Orman, J. A. (2011). High pre-eruptive water contents preserved in lunar melt inclusions. *Science*, *333*(6039), 213–215. https://doi.org/10.1126/science.1204626

Hawke, B., Coombs, C., Gaddis, L., Lucey, P., & Owensby, P. (1989). Remote sensing and geologic studies of localized dark mantle deposits on the Moon. Paper presented at Lunar and Planetary. *Science Conference Proceedings*, Houston, TX.

Head, J., III, & Wilson, L. (1979). Alphonsus-type dark-halo craters-Morphology, morphometry and eruption conditions. Paper Presented at Lunar and Planetary. *Science Conference Proceedings*, Houston, TX.

Head, J. W. (1974). Lunar dark-mantle deposits-possible clues to the distribution of early mare deposits. Paper Presented at Lunar and Planetary. *Science Conference Proceedings*, Houston, TX.

Head, J. W., & Wilson, L. (2017). Generation, ascent and eruption of magma on the Moon: New insights into source depths, magma supply, intrusions and effusive/explosive eruptions (Part 2: Predicted emplacement processes and observations). *Icarus*, *283*, 176–223. https://doi.org/10.1016/j.icarus.2016.05.031

Heiken, G. H., Vaniman, D. T., & French, B. M. (1991). *Lunar sourcebook-A user's guide to the moon, Research supported by NASA* (p. 753). Cambridge, UK:Cambridge University Press.

Heiken, G., & McKay, D. (1977). *Model for eruption behavior of a volcanic vent in Eastern Mare Serenitatis*. Los Alamos, NM: Los Alamos Scientific Lab.

Hess, P. C., & Parmentier, E. (1995). A model for the thermal and chemical evolution of the Moon's interior: Implications for the onset of mare volcanism. *Earth and Planetary Science Letters*, *134*(3–4), 501–514. https://doi.org/10.1016/0012-821x(95)00138-3

Huber, C., & Su, Y. (2015). A pore-scale investigation of the dynamic response of saturated porous media to transient stresses. *Geofluids*, *15*(1–2), 11–23. https://doi.org/10.1111/gfl.12087

Hui, H., Guan, Y., Chen, Y., Peslier, A. H., Zhang, Y., Liu, Y., et al. (2017). A heterogeneous lunar interior for hydrogen isotopes as revealed by the lunar highlands samples. *Earth and Planetary Science Letters*, *473*, 14–23. https://doi.org/10.1016/j.epsl.2017.05.029

Jawin, E. R., Besse, S., Gaddis, L. R., Sunshine, J. M., Head, J. W., & Mazrouei, S. (2015). Examining spectral variations in localized lunar dark mantle deposits. *Journal of Geophysical Research: Planets*, *120*, 1310–1331. https://doi.org/10.1002/2014JE004759

Krumbein, W. C. (1934). Size frequency distributions of sediments. *Journal of Sedimentary Research*, *4*(2), 65–77.

Li, S., & Milliken, R. E. (2016). An empirical thermal correction model for Moon Mineralogy Mapper data constrained by laboratory spectra and Diviner temperatures. *Journal of Geophysical Research: Planets*, *121*, 2081–2107. https://doi.org/10.1002/2016JE005035

Li, S., & Milliken, R. E. (2017). Water on the surface of the Moon as seen by the Moon Mineralogy Mapper: Distribution, abundance, and origins. *Science advances*, *3*(9), e1701471. https://doi.org/10.1126/sciadv.1701471

Lock, S. J., Stewart, S. T., Petaev, M. I., Leinhardt, Z., Mace, M. T., Jacobsen, S. B., & Cuk, M. (2018). The origin of the Moon within a terrestrial synestia. *Journal of Geophysical Research: Planets*, *123*, 910–951. https://doi.org/10.1002/2017JE005333

Longhi, J. (1992). Experimental petrology and petrogenesis of mare volcanics. *Geochimica et Cosmochimica Acta*, *56*(6), 2235–2251. https://doi.org/10.1016/0016-7037(92)90186-m

Longhi, J. (2006). Petrogenesis of picritic mare magmas: Constraints on the extent of early lunar differentiation. *Geochimica et Cosmochimica Acta*, *70*(24), 5919–5934. https://doi.org/10.1016/j.gca.2006.09.023

Lucey, P., Korotev, R. L., Gillis, J. J., Taylor, L. A., Lawrence, D., Campbell, B. A., et al. (2006). 2. Understanding the lunar surface and space-moon interactions. *Reviews in Mineralogy and Geochemistry*, *60*, 83–219. https://doi.org/10.1515/9781501509537-006

McCubbin, F. M., Steele, A., Hauri, E. H., Nekvasil, H., Yamashita, S., & Hemley, R. J. (2010). Nominally hydrous magmatism on the Moon. *Proceedings of the National Academy of Sciences of the United States of America*, *107*(25), 11223–11228. https://doi.org/10.1073/pnas.1006677107

McCubbin, F. M., Steele, A., Nekvasil, H., Schnieders, A., Rose, T., Fries, M., et al. (2010). Detection of structurally bound hydroxyl in fluorapatite from Apollo Mare basalt 15058, 128 using TOF-SIMS. *American Mineralogist*, *95*(8–9), 1141–1150. https://doi.org/10.2138/am.2010.3448

Milliken, R. E. (2006). *Estimating the water content of geologic materials using near-infrared reflectance spectroscopy: Applications to laboratory and spacecraft data* (Ph.D. thesis, p. 404). Brown University, Providence, RI.

Milliken, R. E., & Li, S. (2017). Remote detection of widespread indigenous water in lunar pyroclastic deposits. *Nature Geoscience*, *10*(8), 561–565. https://doi.org/10.1038/ngeo2993

Milliken, R. E., & Mustard, J. (2007a). Estimating the water content of hydrated minerals using reflectance spectroscopy. I: Effects of darkening agents and low-albedo materials. *Icarus*, *189*(2), 550–573. https://doi.org/10.1016/j.icarus.2007.02.017

Milliken, R. E., & Mustard, J. (2007b). Estimating the water content of hydrated minerals using reflectance spectroscopy. II: Effects of particle size. *Icarus*, *189*(2), 574–588. https://doi.org/10.1016/j.icarus.2006.12.028

Milliken, R. E., & Mustard, J. F. (2005). Quantifying absolute water content of minerals using near-infrared reflectance spectroscopy. *Journal of Geophysical Research*, *110*, E12001. https://doi.org/10.1029/2005JE002534

Mueller, S. B., Houghton, B. F., Swanson, D. A., Poret, M., & Fagents, S. A. (2019). Total grain size distribution of an intense Hawaiian fountaining event: Case study of the 1959 Kīlauea Iki eruption. *Bulletin of Volcanology*, *81*(7), 43. https://doi.org/10.1007/s00445-019-1304-y

Robinson, K. L., Barnes, J. J., Nagashima, K., Thomen, A., Franchi, I. A., Huss, G. R., et al. (2016). Water in evolved lunar rocks: Evidence for multiple reservoirs. *Geochimica et Cosmochimica Acta*, *188*, 244–260. https://doi.org/10.1016/j.gca.2016.05.030

Rutherford, M. J., Head, J. W., Saal, A. E., Hauri, E., & Wilson, L. (2017). Model for the origin, ascent, and eruption of lunar picritic magmas. *American Mineralogist*, *102*(10), 2045–2053. https://doi.org/10.2138/am-2017-5994

Saal, A. E., Hauri, E. H., Cascio, M. L., Van Orman, J. A., Rutherford, M. C., & Cooper, R. F. (2008). Volatile content of lunar volcanic glasses and the presence of water in the Moon's interior. *Nature*, *454*(7201), 192–195. https://doi.org/10.1038/nature07047

Saal, A. E., Hauri, E. H., Van Orman, J. A., & Rutherford, M. J. (2013). Hydrogen isotopes in lunar volcanic glasses and melt inclusions reveal a carbonaceous chondrite heritage. *Science*, *340*(6138), 1317–1320. https://doi.org/10.1126/science.1235142

Shearer, C. K., Hess, P. C., Wieczorek, M. A., Pritchard, M. E., Parmentier, E. M., Borg, L. E., et al. (2006). 4. Thermal and magmatic evolution of the moon. *Reviews in Mineralogy and Geochemistry*, *60*(1), 365–518. https://doi.org/10.1515/9781501509537-008

Shearer, C. K., & Papike, J. J. (1993). Basaltic magmatism on the Moon: A perspective from volcanic picritic glass beads. *Geochimica et Cosmochimica Acta*, *57*(19), 4785–4812. https://doi.org/10.1016/0016-7037(93)90200-g

Tartèse, R., Anand, M., Barnes, J. J., Starkey, N. A., Franchi, I. A., & Sano, Y. (2013). The abundance, distribution, and isotopic composition of hydrogen in the Moon as revealed by basaltic lunar samples: Implications for the volatile inventory of the Moon. *Geochimica et Cosmochimica Acta*, *122*, 58–74. https://doi.org/10.1016/j.gca.2013.08.014

Tartèse, R., Anand, M., McCubbin, F. M., Elardo, S. M., Shearer, C. K., & Franchi, I. A. (2014). Apatites in lunar KREEP basalts: The missing link to understanding the H isotope systematics of the Moon. *Geology*, *42*(4), 363–366. https://doi.org/10.1130/g35288.1

Trang, D., Gillis-Davis, J. J., Lemelin, M., Cahill, J. T. S., Hawke, B. R., & Giguere, T. A. (2017). The compositional and physical properties of localized lunar pyroclastic deposits. *Icarus*, *283*, 232–253. https://doi.org/10.1016/j.icarus.2016.09.025

Watson, E., & Bender, J. (1980). Diffusion of cesium, samarium, strontium, and chlorine in molten silicate at high temperatures and pressures. *Paper Presented at Geological Society American Abstract Program*.

Weitz, C. M., Head, J. W., III, & Pieters, C. M. (1998). Lunar regional dark mantle deposits: Geologic, multispectral, and modeling studies. *Journal of Geophysical Research*, *103*(E10), 22725–22759. https://doi.org/10.1029/98JE02027

Wendlandt, R. F. (1991). Oxygen diffusion in basalt and andesite melts: Experimental results and discussion of chemical versus tracer diffusion. *Contributions to Mineralogy and Petrology*, *108*(4), 463–471. https://doi.org/10.1007/BF00303450

Wetzel, D. T., Hauri, E. H., Saal, A. E., & Rutherford, M. J. (2015). Carbon content and degassing history of the lunar volcanic glasses. *Nature Geoscience*, *8*(10), 755–758. https://doi.org/10.1038/ngeo2511

Wetzel, D. T., Rutherford, M. J., Jacobsen, S. D., Hauri, E. H., & Saal, A. E. (2013). Degassing of reduced carbon from planetary basalts. *Proceedings of the National Academy of Sciences of the United State of America*, *110*(20), 8010–8013. https://doi.org/10.1073/pnas.1219266110

Wieczorek, M. A., Neumann, G. A., Nimmo, F., Kiefer, W. S., Taylor, G. J., Melosh, H. J., et al. (2013). The crust of the Moon as seen by GRAIL. *Science*, *339*(6120), 671–675. https://doi.org/10.1126/science.1231530

Wilson, L. (1972). Explosive volcanic eruptions-II the atmospheric trajectories of pyroclasts. *Geophysical Journal International*, *30*(4), 381–392. https://doi.org/10.1111/j.1365-246x.1972.tb05822.x

Wilson, L. (1980). Relationships between pressure, volatile content and ejecta velocity in three types of volcanic explosion. *Journal of Volcanology and Geothermal Research*, *8*(2–4), 297–313. https://doi.org/10.1016/0377-0273(80)90110-9

Wilson, L., & Head, J., III (2003). Deep generation of magmatic gas on the Moon and implications for pyroclastic eruptions. *Geophysical Research Letters*, *30*(12), 1605. https://doi.org/10.1029/2002GL016082

Wilson, L., & Head, J. W. (2017). Generation, ascent and eruption of magma on the Moon: New insights into source depths, magma supply, intrusions and effusive/explosive eruptions (Part 1: Theory). *Icarus*, *283*, 146–175. https://doi.org/10.1016/j.icarus.2015.12.039

Wilson, L., & Keil, K. (2012). Volcanic activity on differentiated asteroids: A review and analysis. *Geochemistry*, *72*(4), 289–321. https://doi.org/10.1016/j.chemer.2012.09.002

Wilson, L., Keil, K., & McCOY, T. J. (2010). Pyroclast loss or retention during explosive volcanism on asteroids: Influence of asteroid size and gas content of melt. *Meteoritics & Planetary Science*, *45*(8), 1284-1301.

Zhang, Y., & Stolper, E. M. (1991). Water diffusion in a basaltic melt. *Nature*, *351*(6324), 306–309. https://doi.org/10.1038/351306a0